Cement and Concrete Research 187 (2025) 107708

Contents lists available at ScienceDirect

Cement and Concrete Research

journal homepage: www.elsevier.com/locate/cemconres

CementFF4: Formal atomic charge polarizable force field for cementitious systems – Bulk and surface

Ziga Casar [a,*,1], Tecla Bottinelli Montandon [a], Manuel Cordova [b], Karen Scrivener [a], Paul Bowen [a], Aslam Kunhi Mohamed [c,2]

[a] *Laboratory of Construction Materials, Institut des Matériaux, Ecole Polytechnique Fédérale de Lausanne (EPFL), CH-1015 Lausanne, Switzerland*
[b] *Laboratory of Magnetic Resonance, Institut des Sciences et Ingénierie Chimiques, Ecole Polytechnique Fédérale de Lausanne (EPFL), CH-1015 Lausanne, Switzerland*
[c] *Institute for Building Materials, Department of Civil, Environmental and Geomatic Engineering, ETH Zürich, CH-8093 Zürich, Switzerland*

ARTICLE INFO

Keywords:
Cement force field
Molecular simulation
Force field (FF)
Cementitious systems
Molecular dynamics
Calcium silicate hydrate

ABSTRACT

A general-purpose formal charge polarizable force field for cementitious systems, CementFF4, is presented. The force field includes the following species: Ca, Si, O, H, Al, Zn, OH^- and H_2O. The force field is a significant extension of previous force fields and is validated by comparison of structural features, elastic constants, reaction enthalpies, and vibrational density of states to experimental and ab initio values for known crystals. Particular attention is given to the tobermorite 14 Å structure, due to its similarity to the main hydration phase of Portland cements, calcium silicate hydrate. The results are in very good agreement with experimental and ab initio data over the entire range of simulated properties (less than 5 % deviation on structural properties and less than 10 % on mechanical properties for non-hydroxide minerals).

1. Introduction

Concrete is a composite material composed of aggregates, anhydride and hydrated phases. At the nanoscale it has a complex, multicomponent, porous, and disordered structure. This complex structure controls many aspects of cement hydration, such as dissolution of anhydride phases, growth of hydrated phases as well as ion transport through the cement paste matrix [1–3]. Given that this complexity imposes constraints on the capabilities of experimental techniques, researchers are increasingly employing computational material science methods to uncover the fundamental mechanisms of cement hydration [2,4–7]. So far molecular modeling of bulk structures has helped elucidate the structural, mechanical, and thermal properties of anhydride and hydrated phases [8–14]. The investigation of interfaces can give an insight into the reactivity and hence the dissolution mechanism [5]. A long-standing challenge remains the study of the main hydration phase, calcium silicate hydrate (C-S-H). Due to the nanocrystalline nature of C-S-H, the proposed molecular models need to be of nanometer size [5,15,16], which hinders the use of ab initio methods, such as density functional theory.

The framework of classical molecular dynamics (MD) provides a good approximation of the physical world to explore the bulk [2,10–13,17,18] as well as the surface [7,15,19–21] properties of cementitious materials at the molecular level. However, the accuracy of MD simulations is determined by the accuracy of the underlying force field (FF), which is a collection of empirical interatomic potentials that describes the forces between atoms. For a detailed review of interatomic potentials, we refer the reader to the excellent review of Müser et al. [22]. In cementitious systems, several FFs have been developed and used, each with its advantages and limitations [23].

No FF is truly versatile, transferable and without limitations. For example, the popular general FF CSH-FF (the further refined version of ClayFF, tailored for simulations of calcium silicate hydrates) [24–26] does not have bond and angle parameters in silica parametrization. Due to missing angle parameters, the required partial charges of oxygens are higher than predicted by DFT, which can lead to unphysically strong electrostatic interaction, consequently overpredicting adsorption phenomena on surfaces [22,27]. A common practice is to use rigid surfaces or frozen bulk structures when investigating interfacial phenomena [21,28–30], because the FFs fail to maintain the desired surface

---

* Corresponding author.
E-mail address: casar.ziga@outlook.com (Z. Casar).
[1] Current address: Department of Chemistry, Durham University, South Road, Durham DH1 3LE, United Kingdom.
[2] Current address: Department of Civil Engineering, IIT Madras, Chennai 600036, Tamil Nadu, India.

https://doi.org/10.1016/j.cemconres.2024.107708
Received 12 May 2024; Received in revised form 16 September 2024; Accepted 23 October 2024

structure. This limits the mobility induced by the vibration of surface atoms, which again influences adsorption phenomena as well as slip along a surface [31,32]. However, non-general FFs were developed to address these issues, such as the Interface Force Field (IFF) [33,34]. These FFs are precisely fitted to a small set of structures, therefore limited in transferability. The shared disadvantage of all these FFs is the lack of polarization.

Valavi et al. [35] recently published the Erica FF2, a formally charged polarizable FF, which is developed from the CementFF family [11,20,23]. Erica FF2 predicts the bulk properties of cementitious materials with high accuracy. The main advantage of this force field is the inclusion of the polarization of silicate oxygens, which results in an improved description of the local atomic environment. Without the polarizable silicate oxygens, the calcium atoms in the main layer of calcium silicate hydrates are undercoordinated. Erica FF2 uses mainly the Buckingham interatomic potential, which is appreciated as a more stable function in comparison to the Lennard-Jones (LJ) potential due to its exponential-6 term [36]. The disadvantages of the Erica FF2 are the small time-step required due to the adiabatic core-shell (ACS) model for polarization [37], the use of the flexible SPC/Fw water model [38] and the Buckingham interatomic potential. Most empirical FFs are of LJ format, which allows for the use of mixing rules, therefore allowing good transferability of interatomic potentials between different FFs. Since there are no mixing rules between Buckingham and LJ potentials, Erica FF2 is thus limited in its potential to simulate systems with atomic species beyond Ca, Si, O and H.

In this paper we present further development and refinement of Erica FF2 [35], named CementFF4, to address the previously mentioned shortcomings. We present a systematic procedure to include metals based on potential parameters from Lewis and Catlow [39]. Zinc interatomic potentials were developed and validated on known structures and used to successfully predict the local atomic environment of zinc incorporated into the C-S-H structure [12]. The adiabatic core-shell model [37] for polarization is refined and leads to energetically more stable structures over longer simulation times. In the spirit of transferability, the key interacting ionic species of C-S-H (Ca^{2+} and OH^-) are fitted to the LJ potential form, which allows for the use of mixing rules when studying interphase phenomena at the solid-liquid C-S-H interface [15]. Finally, the TIP4P/2005 water model [40] is re-adopted as in CementFF3 [11], due to its superior ability to predict bulk solution properties as well as interactions at the surfaces [41,42].

2. CementFF4 parametrization

Force field development can be classified into two approaches: top-down and bottom-up [22]. In the bottom-up approach, any electronic structure calculation is used to provide analytical results and/or small-scale data, such as forces on individual atoms as a function of the atomic configuration. Interatomic potentials are developed with the goal to replicate this information. In the top-down approach, no atomic-scale information is provided. The properties to which the interatomic potentials are fitted are collective, macroscopic properties, such as unit cell parameters and pair distribution functions of known crystal structures, elastic properties, surface energies or phase transitions.

Both approaches are complementary to each other. By using both simultaneously, it is possible to minimize the risk of overfitting [22]. Thus, we employed both approaches. For top-down validation we compare the CementFF4 predictions to structural parameters and elastic properties of known crystals. To validate CementFF4 by the bottom-up approach we compare the calculated vibrational density of states (v-DOS) to the ab initio calculated one. All CementFF4 parameters are listed in SI section 1.

The predecessors of CementFF4 (the CementFF family) were developed by carefully combining parameters from existing FFs. The calcium hydroxide parametrization was adopted from Freeman et al. [43] while the silica parametrization was previously used by Tilocca et al. [44] and de Leeuw et al. [45]. Both FFs use the Buckingham potential form ($E_{ij} = A_{ij}e^{-r/\rho_{ij}} - C_{ij}/r^6$) to describe the short-range van der Waals (vdW) interactions between negative-negative and negative-positive ionic species. In addition to the Buckingham potential form Freeman et al. uses the LJ 9-6 potential form ($E_{ij} = 4\varepsilon_{ij}\left[(\sigma_{ij}/r)^9 - (\sigma_{ijs}/r)^6\right]$) for the oxygen-hydrogen interactions.

The resulting CementFF FFs combined the above mentioned interatomic potentials and were extended by the addition of different water models [11,20,35], which were parametrized with the LJ 12-6 potential form ($E_{ij} = 4\varepsilon_{ij}\left[(\sigma_{ij}/r)^{12} - (\sigma_{ijs}/r)^6\right]$), and aluminium interactions of Buckingham potential form. In CementFF4 the latest set of interatomic potentials of the CementFF family was adapted, further developed, and validated as described in the following. The atomic species included in CementFF4 are listed in Table 1.

2.1. Polarizability

Polarizability is the tendency of matter to acquire an electric dipole moment in response to an electric field arising, e.g., from nearby atom clusters [46]. Typically, the effects of electronic polarizability and screening of electrostatic interactions are implicitly incorporated in the effective charges and other empirical parameters of the FF [47]. Non-polarizable FFs are drastically simplified, but still very successful in modeling many complex molecular systems. However, they fail to properly describe structures in which highly polarizable atoms or ions, most notably anions, are in sites that deviate strongly from inversion symmetry. This particularly concerns oxygen in water, as well as in low-temperature tetrahedral network formers like silica [22]. As explained by Müser et al. [22], polarizability is necessary to accurately reproduce bond-angle distributions and the infrared absorption spectra of silica, as well as capture the α-β transition in quartz. Further, polarizability is essential in obtaining accurate energetics in the vicinity of highly polar moieties, small ions, and anisotropic nonpolar environments. Including polarization in the studied systems can also accommodate the local disruption of hydrogen bond networks by anions, such as chloride, as well as to more accurately reproduce the induced dipole moment of the cation-molecule dimers and describe interfacial systems with better accuracy [48]. Lack of polarizability can result in unreliable results for defects [44], therefore it is crucial to include it when investigating C-S-H, which is a highly defective variation of the tobermorite crystal family.

2.1.1. Adiabatic core-shell model

Mitchell and Finchman [44] developed the adiabatic core-shell (ACS) model, a simple method for adding polarizability to a system. The model falls under classical Drude oscillator models, where a pair of point charges represents dipoles of finite length [48]. Contrary to the Drude model, where the electronic induction is represented by the displacement of a charge-carrying massless particle attached to a polarizable atom [48], in ACS the mass of the atom is divided between the core and the shell, which are connected by a harmonic spring (bond).

Table 1
List of atomic species in CementFF4. More details on sources of species parametrization are listed in SI section 1.

Atomic species	Charge [|e|]	Description
Ca	+2.0	Calcium
Si	+4.0	Silicon
O	+0.84819	Core oxygen
O(S)	−2.84819	Shell oxygen
O_W	−1.1128	Water oxygen
H_W	+0.5564	Water hydrogen
O_H	−1.4	Hydroxide oxygen
H	+0.4	Hydroxide hydrogen
Al	+3.0	Aluminium
Zn	+2.0	Zinc

It is expected that the shells respond quickly to the changing electric field experienced by the ions and are allowed to freely oscillate around the core. Through the free oscillation the shells are polarized by the field of the surrounding ions and the local environment of each ion affects its charge distribution [44]. Due to the small shell mass (approximately 1 % of oxygen mass in Erica FF2 [35]) no energy exchange between the core-shell spring and other degrees of freedom should occur as the frequency of the spring is well above the ionic frequencies [44]. However, a drift in the total energy can occur, if the system is not controlled properly [37,44]. The core and the shell each carry their own charge and the sum of charges equals the formal atomic charge [39] (in Erica FF2 the core has a charge of $+0.84819\ |e|$, while the shell has $-2.84819\ |e|$ [35]). Short-range forces only act on shells. There are no Coulombic interactions between cores and shells.

The parameterization of silicates in CementFF4 was adopted from Tilocca et al. [44] and de Leeuw et al. [45], who used the ACS model to add polarizability to the silicate oxygens for studying pure silica, sodium silicate, and soda-lime silicate glasses. They validated the potentials against experimental and ab initio structural data, such as density, radial and angular atomic distributions, coordination environments, and network connectivity. Their results show that the inclusion of polarization effects improves the description of the tetrahedral connectivity and of the local environment surrounding modified Na and Ca cations. With this, they obtained an improved Q^n distribution of the sodium silicate glass. Valavi et al. [35] observed that inclusion of polarizable silicate oxygens drastically improves the local environment surrounding Ca cations in the tobermorite 14 Å structure. The pairwise interactions were described by Buckingham potentials. Short-range forces between Si and other cations are excluded since Si ions are shielded by oxygen atoms surrounding them. In addition to the two-body terms, the three-body forces and harmonic angle terms were included to control the O-Si-O angle. Due to the three-body term, partial covalence effects are approximately accounted for.

2.2. Water model

For water, the predecessor of Erica FF2, namely CementFF3 [11], uses the rigid, 4-point TIP4P/2005 water model [40]. In Erica FF2 the water model was changed to SPC/Fw, which is a flexible 3-point model [38]. The first reason for the change in the water model was due to its good agreement with experimental data on dielectric constant, relaxation times, and thermal properties, as well as good results for transport properties [38,49]. The second reason was the much easier implementation of this model in LAMMPS [50].

The TIP4P/2005 water model is a rigid 4-point model that consists of three fixed point charges and one Lennard-Jones center [40]. The model was parametrized to fit the temperature of maximum density, the stability of several ice polymorphs, and other commonly used target quantities. The model gives an impressive performance for a variety of properties and thermodynamic conditions, positioning itself as one of the most accurate water models [41,42,51,52]. Due to its excellent performance, it became widely popular for the development of FFs describing ions in aqueous solutions [42,52,53]. Further, Döpke et al. [42] compared the transferability of ion parameters from various water models to the TIP4P/2005 model. They showed that many parameters are easily transferable (most notably from the TIP4P/Ew model), which further confirms the wide usefulness of the TIP4P/2005 water model in molecular dynamics simulations. TIP4P/2005 was shown to successfully reproduce surface specific properties, such as surface tension and hydrogen bonding [54]. Since cementitious systems have ubiquitous solid-liquid interfaces, where the aqueous solution is composed of a wide variety of ionic species, we decided to re-adopt the TIP4P/2005 water model in CementFF4.

2.3. Buckingham potentials

Lewis and Catlow [39] published a systematic approach for the derivation of empirical potential parameters for binary oxides. For fitting of the potential parameters, they used the top-down approach, where they fit the experimental data to replicate the structural, elastic, dielectric, and lattice dynamical crystal properties. In their parametrization, they used the ACS model to add polarizability. While they used it for cations and anions, the cation polarizability is less strongly influenced by the crystal environment [22]. The cation-cation interactions are purely Coulombic since cations are shielded by anions in oxides. The cation-anion interactions are described with the Buckingham potential form.

The Zn-O(S) Buckingham interaction of CementFF4 was adopted from Lewis and Catlow [39], the Zn-O_W Lennard-Jones 12-6 interaction was calculated through the mixing rule, and the Zn-O_H Buckingham interaction had to be developed separately. To derive the Zn-O_H Buckingham interaction, we kept the ρ parameter fixed to the value of the Zn-O(S) interaction from Lewis and Catlow [39]. The starting A parameter was chosen as $A = A_{Zn-O(S)} \bullet q_{Oh}/q_O$, where q_i is the charge of the respected oxygen species (q_O is the combined charge of the core-shell pair, $-2\ |e|$) and $A_{Zn-O(S)}$ is the Buckingham parameter of the Zn-O(S) interaction. In an iterative process, the interatomic potential was used in structure prediction of a reference crystal structure. In each iteration, the A parameter was adjusted until the radial distribution function of Zn-O_H agreed with the experimental data. Additionally, a harmonic angle term was introduced for the O_j-Zn-O_i connectivity (where i and j can be O(S) or O_H, respectively) in the zincate tetrahedra. This harmonic angle improved the structural prediction (unit cell parameters) by approximately 5 % and prevented spontaneous 5-fold coordination of zinc. The parameters for the harmonic angle description were also found by a trial-and-error iteration.

2.4. Lennard-Jones 12-6 parametrization

The Buckingham potential form is considered more stable than the LJ potential form [36]. However, the LJ 12-6 potential form is the most widely used pair-potential [55]. One of the main reasons for this is that the individual atomic LJ parameters can be directly used without the need to derive the cross-interaction terms, which are calculated by the MD package depending on the chosen mixing rules. This enables a wide range of well parametrized interatomic potentials which can be easily adapted and used.

In CementFF4, Ca^{2+} and OH^- ions were fitted to the LJ 12-6 potential form, as described below. Further, the LJ 12-6 potential form for Al^{3+} was adopted from the Li et al. [42,56] and is used to model the Al-O_H and Al-O_W interactions. With this, an improved description of the local environment of aluminates was achieved. The Zn^{2+} LJ potential was adopted from Arab et al. [57] and is used to model the Zn-O_W interaction.

The Zn-O_H and all interactions with the silicate oxygens O(S) were kept in Buckingham potential form (see Section 2.4). The Zn-O_H Buckingham potential form predicted the structural features of known crystals with better accuracy than the LJ 12-6 potential form which can be obtained by the mixing rule for Zn^{2+} and $O_H^{1.4-}$. The silicate oxygen interactions were kept in the Buckingham potential form since they would require a completely new reparameterization of the ACS model, pairwise interactions and harmonic angle terms.

In order to fit a LJ 12-6 potential function to the Buckingham one, a starting point had to be selected. First, the mixing rule must be selected, for which we chose the Lorentz-Berthelot rule ($\varepsilon_{ij} = \sqrt{\varepsilon_i \bullet \varepsilon_j}$ and $\sigma_{ij} = \left(\sigma_i + \sigma_j\right)/2$) [58,59]. This rule is widely used in the literature and as long as the σ parameters are similar, the choice of the mixing rule has minimum effect on the result [60]. Afterwards the Ca^{2+} LJ parametrization was selected. We chose the parametrization (ε_{Ca} and σ_{Ca}) from

Mamatkulov et al. [61], since it predicts the experimental hydration free energy, coordination number, ion-oxygen distance, and self-diffusion coefficient of Ca^{2+} in water with good accuracy [42]. At this stage we used the SciPy Python library [62], to fit the LJ potential function (adjustable parameters: ε_{Ca-Oh} and σ_{Ca-Oh}) to the Buckingham potential form (A_{Ca-Oh}, ρ_{Ca-Oh} and C_{Ca-Oh}) from Freeman et al. [43]. The fitting resulted in ε_{Oh} and σ_{Oh}, which were further refined in order to correctly predict the portlandite crystal structure.

With the obtained ε_{Oh} and σ_{Oh} the Al-O_H and O_W-O_H were calculated using the Lorentz-Berthelot mixing rule (see SI section 1).

3. Methods

3.1. Molecular dynamics

All simulations were carried out with LAMMPS [43]. Unless otherwise stated in the text the simulation duration was at least 10 ns, whereby the reported results are the average of the last 3 ns, after reaching equilibrium. The system was considered in equilibrium if the energies and unit cell parameters fluctuated around constant values for at least 3 ns. All calculations were carried out at constant pressure and temperature (1 atm and 300 K), Noose-Hoover thermostat and barostat, with flexible angles and simulation cell parameters in the case of solids (anisotropic NPT ensemble) and with constant cell geometry in the case of liquids (isotropic NPT ensemble). The time step was 0.28 fs. The kspace solver was the pppm/tip4p solver with a cutoff of 10 Å and an accuracy of $1e^{-4}$ eV, as implemented in LAMMPS.

Simulations of structures which included the ACS model started with a pre-step to equilibrate the core-shells to prevent the drift of total energy, as described in by Mitchel and Fichman [37]. The detailed implementation is given in the LAMMPS documentation [43], explained by Valavi et al. [35] and can be seen in the provided LAMMPS input files in the SI. The duration of this pre-equilibration can be as short as 1000 steps.

When calculating the enthalpy of the given system a few corrections need to be considered. LAMMPS calculates the enthalpy as $H = E_{Total} + p \bullet V$. In their calculations the contribution of the core-shell interactions is not added, nor is the energy of the hydroxide bonds. Therefore, the (corrected) enthalpy used for the energetical validation is computed as follows:

$$H_{corr} = H + PE_{Core-Shell} + N_{Oh} \bullet \mathrm{D} \tag{1}$$

where $PE_{Core-Shell}$ is the sum of the potential energy which arises due to the bonding of individual core-shell pairs, N_{Oh} is the number of hydroxyls and D is the depth of the potential well in the Morse potential form ($E_{ij} = D\left[1 - e^{-\alpha(r-r_0)}\right]^2$). The last contribution in Eq. (1) represents the energy correction for each O_H-H bond needed in the LAMMPS implementation of the Morse bond. Historically, the CementFF1 force field was developed in conjunction with the DL Poly molecular simulation package [63]. Since the Morse potential description of DL Poly subtracts the D term ($E_{ij} = D\left[1 - e^{-\alpha(r-r_0)}\right]^2 - D$), the correction is used to enable the comparison of the force fields.

The elastic constants calculations were carried out at finite temperature as implemented in LAMMPS. First the structures were equilibrated for 10 ns. The final atomic configuration of the equilibration was used as the initial configuration for the elastic constant calculation. For the calculation small deformations in the linear regime to the simulation box in the canonical NVT ensemble are applied. The detailed description of the simulation protocol is given in the Erica FF2 paper of Valavi et al. [35].

The vibrational density of states (v-DOS) was calculated with the TRAVIS software [64,65]. The structures were first equilibrated for 20 ns. Afterwards, the trajectories were saved every 0.84 fs over a period of 14 ps, from which the spectra were calculated. The autocorrelation function for the v-DOS calculation was weighted by atomic mass. Global and projected v-DOS were calculated. To exclude the influence of the time step, the length and saving interval of trajectories were varied. No significant differences were observed. The input files for TRAVIS are provided as part of SI.

3.2. DFT elastic constants calculation

The crystal structure of clinohedrite was obtained from Materials project [66] (ID: mp-696,853). All computations were carried out using the plane-wave density functional theory (DFT) software Quantum ESPRESSO, version 6.5 [67,68]. All computations were performed at the PBE level of theory [69] using Grimme D2 dispersion correction [70] and projector augmented wave [71] scalar relativistic pseudopotentials obtained from PSlibrary version 1.0.0 [72]. Wavefunction and charge density energy cutoffs were set to 100 Ry and 800 Ry, respectively. $4 \times 3 \times 2$ and $3 \times 3 \times 1$ Monkhorst-Pack grids of k-points [73] were used for ε-$Zn(OH)_2$ and clinohedrite, respectively.

Elastic constants were obtained using the ElaStic software [74]. The atomic positions and lattice parameters of the initial crystal structures were first optimized while retaining the space group of the crystal structure, then 21 distorted structures with a maximum absolute Lagrangian strain of 0.08 were generated for each deformation type using the ElaStic software. The energy of each distorted structure was obtained after optimization of atomic positions.

For each deformation type, the strain-energy relationship was fitted using 4th or 6th order polynomial functions, discarding points deviating from the expected harmonic behavior at large strain values when required, as described in [74]. All energy-strain curves are shown in SI section 6.

4. Results

The results of the CementFF4 validation are summarized here. First, the equilibration of the ACS model is introduced. Second, the newly developed parameters of CementFF4 are validated on known crystal structures. Third, CementFF4 is tested and compared to other FFs in predicting the adsorption of Ca^{2+} at the SiO_2 surface and predicting the tobermorite 14 Å structure, a crystalline calcium silicate hydrate. Finally, CementFF4 is tested on a C-S-H structure with incorporated zinc, which was relaxed with density functional theory.

4.1. Core-shell equilibration

The original parametrization of the silicates in Erica FF2 uses the ACS model for oxygen atoms. The distribution of mass is 15.79 g/mol on the oxygen core and 0.2 g/mol on the oxygen shell. The validation simulations of Erica FF2 were carried out for 1 ns [35]. A drift in the total energy up till 1 ns was not observed (sm0.2 in Fig. 1a). From longer calculation times (20 ns production run in NPT ensemble) it is evident that an increase in the total energy occurs, roughly at 0.75 eV/ns for tobermorite 14 Å ($4 \times 4 \times 1$ supercell). While the kinetic energy of the system remains constant, the potential energy increases which contributes to the increase of the total energy of the system. When monitoring the movement of the cores and shells an increase in the potential energy of the core-shell pairs is observed (Fig. 1b). This increase can be related to the increase of the kinetic energy (shown as velocity in Fig. 2), since shells that are oscillating around the cores keep gaining momentum, therefore moving further away from the cores.

While it is possible to regulate the system by adjusting the damping parameters of the thermostat and barostat, this had a minimal effect, and it did not prevent the energy drift (see SI Fig. S1). The drift in energy is related to the increase of the core-shell potential energy and can be prevented in one of two ways. First, with a lower time step. If the timestep is decreased from 0.2 fs to 0.1 fs the energy drift does not occur. However, due to the already small time-step (in comparison to nonpolarizable force fields) a further decrease in the time step is not desirable.

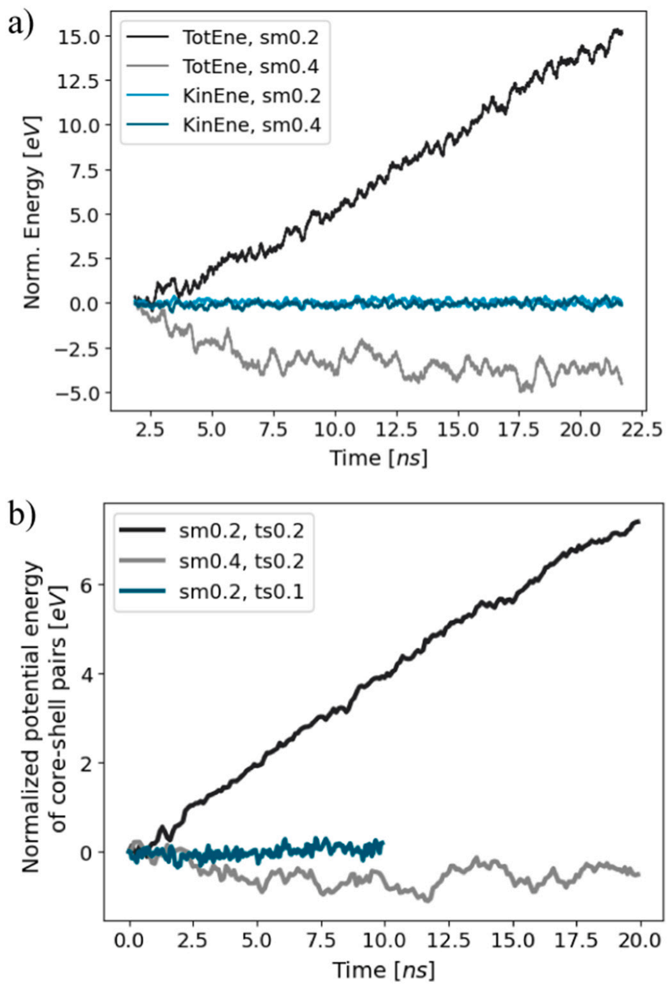

Fig. 1. a) Change of total (TotEne) and kinetic (KinEne) energy of tobermorite 14 Å (4 × 4 × 1 supercell) during the 20 ns production run for shell mass 0.2 g/mol (sm0.2) and 0.4 g/mol (sm0.4); b) total potential energy of all core-shell pairs normalized to the initial value during the 20 ns production run for shell mass 0.2 g/mol (sm0.2) and 0.4 g/mol (sm0.4) for time step values 0.2 fs (ts0.2) and 0.1 fs (ts0.1).

The second approach is by adjusting the mass distribution between the core and the shell. The new mass of the core was set to 15.59 g/mol, while the new mass of the shell was set to 0.4 g/mol. With this, the potential energy of the core-shell pairs and the kinetic energy of the shells remained constant (Figs. 1b and 2a). No structural changes between the different ACS parametrizations in the tobermorite structure were observed (see SI section 3).

4.2. Validation

4.2.1. Structural validation

CementFF4 was used to simulate 12 structures which are relevant for cementitious systems. The structures were chosen as having local atomic arrangements similar to those in cementitious systems. The deviation in unit cell parameters between the MD predicted structures and experimental references is given in Table 2 and the exact values are given in SI section 4. While it is beyond the scope of this paper to discuss the structural details of all compounds considered, some important points are addressed below.

As seen in Table 2, compounds which do not contain hydroxyl groups are successfully predicted by CementFF4. An exception is $Ca_3Al_2O_6$ which deviates from the experimental reference by roughly 5.5 %. This may be attributed to the overestimation of the first shell Al-O distance of the aluminium tetrahedra (calculated 2.00 Å versus experimentally determined 1.75 Å). Other distances (Ca-O, Al-Ca) are in good agreement with the experiments (deviation below 2 %). However, the octahedral Al polyhedra in Al_2O_3 are accurately modeled (Al-O distance calculated 1.91 Å versus experimental 1.91 Å).

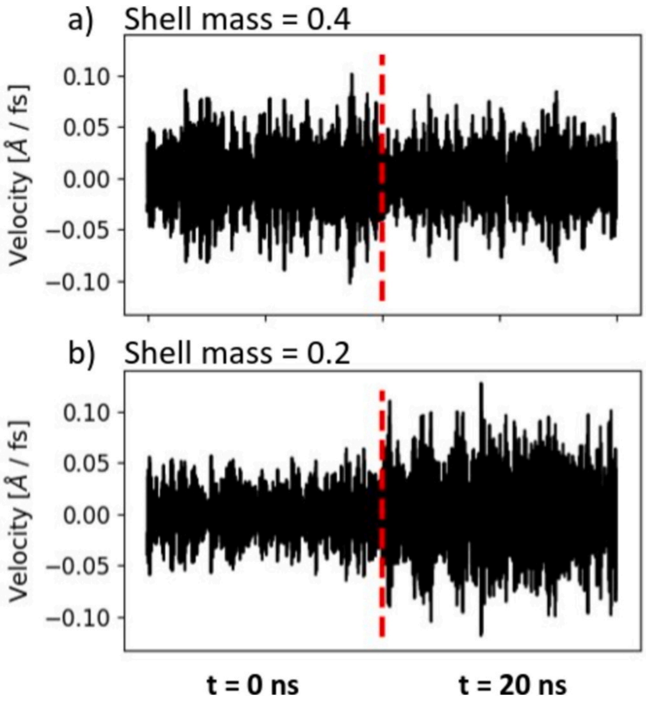

Fig. 2. The relative velocity of the shell to the core. a) Shell mass 0.4 g/mol and b) shell mass 0.2 g/mol. The left side of each graph is the relative velocity of the shell at the start of the equilibration run and on the right side the relative velocity of the shell at the end of the production run (at 20 ns).

Table 2
Structural validation of CementFF4. The deviation of unit cell parameters between MD predicted structures and references is given. The exact values and references are given in Table S8.

Structure	a dev	b dev	c dev	α dev	β dev	γ dev
CaO Lime	0.18 %	0.19 %	0.19 %	0.00 %	0.00 %	0.00 %
$Ca(OH)_2$ Portlandite	2.24 %	2.24 %	−4.12 %	0.00 %	0.00 %	0.00 %
γ-$Al(OH)_3$ Gibbsite	10.56 %	9.15 %	−16.54 %	−0.60 %	1.34 %	0.00 %
$Ca_3Al_2O_{12}H_{12}$ Hydrogarnet	7.87 %	7.87 %	7.87 %	0.00 %	0.00 %	0.00 %
SiO_2 Quartz	0.05 %	0.05 %	2.58 %	0.00 %	0.00 %	0.00 %
$Ca_3Al_2O_6$ Tricalcium aluminate	5.18 %	0.04 %	5.47 %	−0.08 %	−0.10 %	0.04 %
$CaSiZnO_5H_2$ Clinohedrite	2.06 %	0.76 %	0.07 %	0.00 %	1.98 %	0.01 %
$CaZn_2Si_2O_7{\cdot}H_2O$ Junitoite	2.33 %	−1.46 %	0.17 %	−2.66 %	−0.02 %	0.50 %
$Ca_2Si_2ZnO_7$ Hardystonite	2.50 %	2.50 %	−0.52 %	0.01 %	0.00 %	0.00 %
Zn_2SiO_4 Willemite	−1.14 %	−1.14 %	1.31 %	0.00 %	0.00 %	0.00 %
ZnO Zincite	−1.00 %	−1.00 %	−0.89 %	0.00 %	0.00 %	0.01 %
ε-$Zn(OH)_2$	9.53 %	4.40 %	−5.74 %	−0.01 %	−0.03 %	−2.24 %
β-$Zn(OH)_2$ Zinc hydroxide	1.57 %	1.57 %	4.42 %	0.00 %	0.00 %	0.00 %

4.2.1.1. Hydroxides. The first hydroxide of interest is portlandite ($Ca(OH)_2$), due to its importance in cement hydration. The crystalline structure of portlandite is today very well-known [75]. As seen in Table 2, the MD unit cell is 2.24 % larger in the *a*- and *b*-direction, while it is 4.12 % smaller in the *c*-direction compared to the reference structure. This is comparable to Erica FF2 where the overestimate in the *a*- and *b*-directions was 2.18 % and the underestimation in *c*-direction was 3.85 %. A closer examination of the radial distribution functions (RDF, see SI section 3) reveals a good match of the first peaks of Ca-O_H RDF (2.41 Å for MD, and 2.38 Å experimental) and Ca-H RDF (2.98 Å for MD and experiment). The calcium atoms are octahedrally coordinated to six oxygen atoms, which was captured by the FF. The structural difference becomes evident after analyzing the O_H-O_H RDF, where the FF predicts the first peak at 3.2 Å, while the experimental O_H-O_H distance is 3.05 Å. This peak corresponds to the smallest distance of two oxygens inside the same calcium octahedra. The structure of portlandite consists of stacked $[Ca(OH)_6]$ layers lying in the (001) plane. The layers interact mainly through weak H-mediated dispersive forces [75]. The second peak (3.3 Å) of the experimental O_H-O_H corresponds to the oxygen atoms of neighboring layers and is missing from the computed RDF. This also explains the larger deviation in the c-direction. While CementFF4 accurately predicts the distances of the first coordination shell, it less accurately describes the interactions between the hydrogen and oxygen atoms.

Considering gibbsite (γ-$Al(OH)_3$). The resulting deviation of unit cell parameters is roughly 10 %. The predicted structure with the Erica FF2 (and CementFF2 which uses the same Al-O_H interatomic potential) for gibbsite deviates in the *a*, *b* and *c*-direction by 18 %, 23 % and 23 %. CementFF4 predicts the Al-O_H distance at 2.1 Å, while Erica FF2 predicts 1.87 Å. The experimentally measured distance of Al-O_H of the aluminium octahedral is 1.93 Å. While Erica FF2's first shell distance is closer to the experimental value, it predicts a 4-fold aluminium oxygen coordination, whereas gibbsite's aluminium atoms are 6-fold coordinated, which is captured by the new LJ potential form for Al-O_H in CementFF4. The radial distribution functions for gibbsite are given in SI section 7.

There are two different zinc hydroxide ($Zn(OH)_2$) polymorphs: ε-$Zn(OH)_2$ where zinc is tetrahedrally coordinated to four oxygens, and β-$Zn(OH)_2$, where zinc is in octahedral coordination with six oxygens. Similar to gibbsite CementFF4 predicts the ε-$Zn(OH)_2$ structure with relatively large deviations (9.53 %) in the unit cell parameters. However, CementFF4 correctly predicts a 4-fold coordination with an average first shell Zn-O_H distance deviation of 5 % (SI section 7). The structural ordering of the zinc tetrahedra in ε-$Zn(OH)_2$ comes from hydrogen bonds between the hydroxyl groups of neighboring tetrahedra. The origin of the hydrogen bond arises from quantum mechanical effects and not from the classical (exchange free) London dispersion and electrostatic 'dipole-dipole' forces which play only a secondary role [68]. In the LJ potential form the exponential-12 term describes the Pauli repulsion at short distances, while the exponential-6 term describes the London dispersion force (attractive) at long range. Therefore, it is of no surprise that it is difficult to accurately describe structures, which strongly depend on hydrogen bonding.

The structure of β-$Zn(OH)_2$ has a layer hydroxide structure, similar to portlandite. The zinc atoms are 6-fold coordinated to hydroxyl groups. CementFF4 successfully predicts the 6-fold coordination with a deviation of the Zn-O_H first shell distance by 2.5 %. Since hydrogen bonding is only expected between the individual hydroxide layers, it affects the structure much less than that of ε-$Zn(OH)_2$. This is reflected in the prediction of unit cell parameters for β-$Zn(OH)_2$ (Table 2) where the deviation of *a*- and *b*-axis are 1.57 %, and *c*-axis 4.42 %. The deviation of unit cell parameters and the first shell distance are well below the expected values for a hydroxide.

Since the tobermorite structure has a close resemblance to the C-S-H structure it is discussed in a separate section.

4.2.2. *Energetical validation*

A rarely applied but an essential validation that is carried out for CementFF family of FFs is the energetical validation on certain relevant chemical reactions for cementitious systems [20,35]. This not only gives us a way to estimate the error associated with CementFF4 in calculating energies but also ensures the transferability of CementFF4 to a wide range of systems. As classical FFs cannot simulate bond breakage, a correction must be added for any reactions involving the conversion of water and oxide ions into hydroxide ions or vice versa. This correction is calculated using the reactions listed in Table 3. The average correction for each reaction per water molecule is taken as the correction factor for water splitting and is equal to -2.82 eV/H_2O. All the reactions we have selected for the energetic validation are listed in Table 4. The error estimation for these reactions is according to the methodology developed for CementFF1 [20].

The reaction enthalpies are calculated as $\Delta H_{MD} = \sum S_i^P H_i^P - \sum S_i^R H_i^R$, where S_i is the stoichiometry coefficient, H_i is the enthalpy and the superscripts *P* and *R* represent products and reactants, respectively. In the case of aqueous species, the energy of the aqueous species is estimated based on the energy difference between two boxes of water with the same number of water molecules but with and without the aqueous species.

As seen in Table 4 the calculated reactions enthalpies for non-hydroxides are within the error estimation. The reactions of most hydroxides are outside the error estimation. Those reactions are the ones which indicate a transition between a hydroxide and an oxide. As already explained in the Structural validation section, pure hydroxides are very difficult to simulate correctly, due to the limitation of modeling hydrogen bonding with empirical interatomic potentials. Hence the less accurate predictions for these 6 reactions.

4.2.3. *Mechanical validation*

Elastic properties are among the most important properties of solids [77]. Therefore, any interatomic potential should be tested for its ability to reproduce the elastic tensor of crystalline references. The individual components of the elastic tensor (c_{ij}) give a good estimation of the accuracy of CementFF4 and can be used for further development of the FF [78]. However, elastic constants are not uniquely defined, except at zero stress and zero temperature. Different definitions lead to deviations of similar order as the external stress [22]. Further, the discrepancy between individual elastic constants (c_{ij}) determined by different experiments can be higher than 100 % [79].

The interatomic potential from Lewis and Catlow [39], which is used to describe the Zn-O(S) interaction was constructed by fitting the elastic constants of the calculated structures to the experimental ones. This is seen in the excellent agreement between the MD calculated individual components of the elastic tensor with experimental and DFT calculated values for Hardystonite ($Ca_2ZnSi_2O_7$), Zincite (ZnO) and Clinohedrite ($CaZnSiO_4{\cdot}H_2O$). The calculated bulk modulus for Hardystonite and Zincite are within 2 % deviation to the reference data. The bulk modulus of clinohedrite is within 10 % deviation, which can be attributed to the difficulty of modeling materials with confined water (Table 5).

Regarding the elastic constants of portlandite: first, the calculated bulk modulus (K) with the new LJ potential form for Ca-O_H of CementFF4 is closer to experimental measurements than the one calculated with Erica FF2. The improvement in accuracy is due to a better prediction of c_{12} and c_{13} elastic constants. Portlandite exhibits a

Table 3
Reaction for calculated water splitting correction.

Reaction	H_{sim}	H_{exp} [76]	H_{corr}
$Ca(OH)_2 \rightarrow CaO + H_2O$	5.54	0.66	−4.88
$[Si(OH)_4]_{aq} \rightarrow SiO_2 + 2H_2O$	−3.05	−6.27	−1.61
$AlOOH + H_2O \rightarrow Al(OH)_3$	−4.05	−0.11	−3.94
$Al_2O_3 + 3H_2O \rightarrow 2Al(OH)_3$	−3.08	−0.46	−0.87

Table 4
Reactions for energetic validation. Err_{est} is the estimated error as defined by Galmarini et al. [20]. ΔH_{EXP} is taken from [76].

#	Reaction	ΔH_{MD} [eV]	ΔH_{EXP} [eV]	$\lvert\Delta H_{MD}$-$\Delta H_{EXP}\rvert$ [eV]	Err_{est} [eV]
1	$Ca(OH)_2 \rightarrow (Ca^{2+})_{aq} + 2(OH^-)_{aq}$	−0.86	−0.19	0.67	0.61
2	$2H_2O + SiO_2 \rightarrow (Si(OH)_4)_{aq}$	8.70	6.27	2.43	2.30
3	$Ca(OH)_2 + SiO_2 \rightarrow (CaSiO_4H_2)_{aq}$	−2.95	2.44	5.39	0.56
4	$(Ca^{2+} + 2OH^-)_{aq} + (Si(OH)_4)_{aq} \rightarrow (CaSiO_4H_2)_{aq} + 2H_2O$	−12.51	−3.62	8.89	3.12
5	$AlOOH + H_2O \rightarrow Al(OH)_3$	−1.22	−0.11	1.11	1.16
6	$3Ca(OH)_2 + 2Al(OH)_3 \rightarrow Ca_3Al_2(OH)_{12}$	1.88	−0.42	2.30	3.98
7	$3CaO + Al_2O_3 + 6H_2O \rightarrow Ca_3Al_2(OH)_{12}$	−0.88	−2.50	1.62	3.90
8	$3CaO + 2Al(OH)_3 + 3H_2O \rightarrow Ca_3Al_2(OH)_{12}$	−6.28	−5.00	1.28	0.90
9	$Al_2O_3 + 3H_2O \rightarrow 2Al(OH)_3$	5.40	−0.46	5.86	2.56
10	$Ca(OH)_2 \rightarrow CaO + H_2O$	2.72	0.66	2.06	0.72
11	$2Ca(OH)_2 + SiO_2 \rightarrow 2CaO + (Si(OH)_4)_{aq}$	14.14	7.6	6.54	3.66

large elastic anisotropy in compressional (c_{11} and c_{33}) and shear elastic coefficients (c_{66} and c_{44}). This corresponds to a larger stiffness and rigidity in the basal plane with respect to the axial direction [79]. As seen in Table 5, the shear elastic coefficients predicted with CementFF4 are in better agreement with the experimental data than the compressional coefficients. The overestimation of the compressional coefficients can be related to the predicted structural characteristics of portlandite, where the underestimate in the *c*-direction hints at a stronger interaction from the MD compared to the experiment between the basal [$Ca(OH)_6$] layers, resulting in higher compressional coefficients.

4.2.4. Ion-surface interaction

In order to evaluate the adsorption of Ca^{2+} on silicate surfaces CementFF4 is compared to the FF used by Bischoff et al. [81]. In this study, they successfully combined molecular dynamics and polarimetric angle-resolved second harmonic scattering to explore ion-specific adsorption effects at the SiO_2 quartz (101) surface. The FF used is a classical FF which uses the Lennard-Jones potential form and employs partial charges [41,82].

The simulation box used (see Fig. S4) was of size 5.5, 3.9, and 8.0 nm in the *x*-, *y*-, and *z*-axis directions. A slab of solution was placed in the middle of the simulation box (3762 water molecules, 24 Ca^{2+} and 16 Cl^- ions), which was enclosed on each side, in the *z*-axis direction, with 4 layers of crystalline SiO_2. While the simulation box had periodic boundary conditions in the *x*- and *y*-axis direction, it had a fixed wall boundary condition in *z*-axis. The fixed wall was used to prevent artificial polarization due to periodicity effects in the treatment of electrostatic interactions [32]. On each surface 12.5 % of the silanol groups were deprotonated (16 out of 128 per surface) with this a negative surface charge was achieved. The choice of comparing the FFs in a system with a negative surface charge (deprotonation of silanol groups) since similar conditions are expected for C-S-H [83,84]. Except for the surface silicate layer, the bulk SiO_2 structure was frozen. Identical initial structures were used for both FFs. The simulations were 50 ns long, with the results averaged over the last 4 ns. The plotted density profiles were averaged over each half of the simulation box. The simulation was carried out in the canonical (NVT) ensemble at 300 K.

To compare the results of the distribution of Ca^{2+} between inner-sphere, outer-sphere, diffuse layer, and bulk solution were examined. The results are shown in Table 6. Inner-sphere adsorption is considered if a Ca^{2+} is closer than 3.15 Å to a silicate oxygen, and outer-sphere if closer than 5.15 Å. Ions are counted as being in the diffuse layer if they're not inner or outer-sphere adsorbed but less than 15 Å from the surface (*z*-axis direction) [81]. All remaining ions are considered as part of the bulk of the solution. The amount of inner and outer-sphere adsorbed Ca^{2+} predicted by both FFs is comparable. A difference is observed in the structuring of the diffuse layer and bulk solution, where the FF from Bischoff et al. favors Ca^{2+} in the bulk of solution over the diffuse layer. The difference could be partially attributed to CementFF4's tendency to adsorb a small amount of Cl^- ions close to the SiO_2 surface, as seen in Fig. 3. Adsorption of Cl^- due to the attraction to positively charged hydrogens of silanol groups increases the negative charge close to the surface, which could attract more Ca^{2+}.

Second harmonic scattering is a valuable experimental technique to probe the interface of a particle [85]. In their study, Bischoff et al. [81] successfully correlated their experimental findings with atomistic

Table 6
Percentage of adsorbed Ca^{2+} by type of adsorption.

	Inner-sphere	Outer-sphere	Diffuse layer	Bulk solution
CementFF4	22.4 %	17.7 %	41.4 %	18.5 %
Bischoff et al. [81]	23.0 %	13.3 %	18.2 %	45.5 %

Table 5
Elastic constants cij in Voigt notation. All constants are in GPa. For hardystonite average c is reported in brackets, calculated as $c = (c_{11} + c_{12} + c_{13} + c_{33} + c_{44} + c_{66})/6$. K is the bulk modulus and G is the shear modulus. Zincite DFT calculated values are from The Materials Project entry mp-2133 [66].

	c_{11}	c_{12}	c_{13}	c_{22}	c_{33}	c_{44}	c_{66}	G_1	G_2	K
Hardystonite	164.4	77.6	54.0		168.7	16.0	63.0	40.1	51.5	98.3 (90.3)
Exp [72]	163.3	81.0	55.3	–	159.9	29.9	57.3	–	–	–(88.4)
Zincite	221.5	88.9	88.0	224.3	193.4	71.6	67.4	63.1	71.3	128.9
Exp [73]	209.7	121.1	105.1	–	210.9	41.5	44.3	–	–	–
DFT [58]	188.0	109.0	92.0	188.0	205.0	37.0	39.0	42.0	–	130
Clinohedrite	187.4	60.4	79.4	131.1	172.1	55.8	59.9	56.6	45.8	102.4
DFT	142.6	64.7	58.5	183.4	122.6	49.7	38.0	–	45.5	93.2
Portlandite	168.2	44.9	8.1	165.5	32.0	16.5	56.5	29.3	49.0	56.6
Erica FF2	159.4	81.2	20.2	156.9	32.8	3.8	42.0	18.4	37.3	66.5
DFT [80]	99.39	30.78	7.36	–	36.29	7.88	34.31	–	–	36.46
Exp [74]	99.3	36.2	29.7	–	32.6	9.9	31.6	–	–	46.9
Exp [71]	102.0	32.0	8.4	–	33.6	12.0	34.3	–	–	36.4
Tobermorite	111.2	38.4	20.3	112.7	66.3	2.4	44.4	20.2	35.3	49.7
Erica FF2 [27]	99.4	46.4	19.0	130.7	60.6	26.2	39.4	24.0	35.2	49.9
DFT [9]	–	–	–	–	–	–	–	–	–	49.0
DFT [75]	77.6	35.9	20.18	104.5	32.05	24.5	38.1	24.1	–	42.1
Exp [76]	–	–	–	–	–	–	–	–	–	47 ± 4

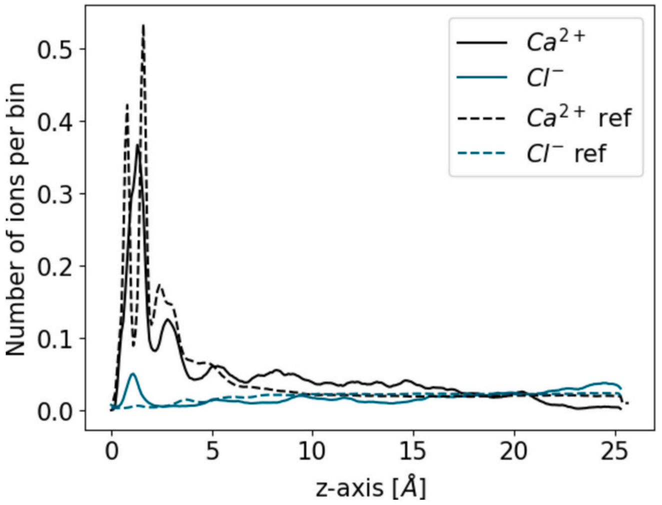

Fig. 3. Ion distribution through the solution slab. The reference results correspond to the FF used by Bischoff et al. [81].

simulations which were carried out with a specialized FF. The comparable amount of inner- and outer-sphere adsorbed Ca^{2+} by CementFF4, a formal atomic charge polarizable force field, to a specialized FF [81] is a reassuring measure. The difference in the number of Ca^{2+} in the diffuse layer and bulk of solution is presumably related to the choice of the water model (SPC/E versus TIP4P/2005) and the ionic charges. While the charge of Ca^{2+} in CementFF4 is set to the formal charge +2 |e|, Bischoff et al. [81] used the electronic continuum correction method whereby the charges were scaled to 75 % of their formal value (+1.5 |e|). The scaling of charges implicitly adds electronic polarization to the system [41] which in CementFF4 is not accounted for beyond silicate oxygens.

4.3. *Calcium silicate hydrates*

4.3.1. *Tobermorite 14 Å*

FFs which are meant to study the main cement hydration phase C-S-H should always be compared with respect to the structures of the tobermorite crystal family. In particular to tobermorite 14 Å, due to its resemblance with the C-S-H structure [2,86,87]. Calculations were carried out on a tobermorite 14 Å super cell of 4 × 4 × 1 crystalline unit cells [88]. The simulation details are given in the Methods section.

Table 7 reports the deviation of unit cell parameters with respect to experimental data from Bonaccorsi et al. [88] for four FFs: the widely used non-polarizable ClayFF [25,26] and CSH-FF [24], Erica FF2 [35] and CementFF4. As seen ClayFF and CSH-FF fail to replicate the unit cell of tobermorite, particularly the *c*-direction, where an expansion of the interlayers occurs. Erica FF2 replicates the unit cell with satisfactory accuracy, with a 4 % deviation in the β angle. CementFF4 differs from Erica FF2 in the use of the TIP4P/2005 water model, as well as Ca-O_H, Ca-O_W and O_H-O_W interactions. The change of those parameters improved the prediction of the unit cell.

Table 7
Comparison of the deviation of unit cell parameters between the experimental value [88] and as predicted by different force fields.

Force field	a dev	b dev	c dev	α dev	β dev	γ dev
CSH-FF [24]	8.98 %	8.41 %	17.03 %	−1.62 %	−3.15 %	0.58 %
ClayFF [26]	10.70 %	9.09 %	12.70 %	−8.80 %	−15.10 %	0.60 %
Erica FF2 [35]	−0.05 %	0.55 %	1.51 %	−0.59 %	4.01 %	0.31 %
CementFF4	−0.15 %	0.38 %	1.61 %	−0.27 %	−0.12 %	0.26 %

The calculated pair distribution function (PDF, Fig. 4) shows an excellent agreement for Erica FF2 and CementFF4 with the experimentally reported distances [88]. ClayFF and CSH-FF fail to correctly describe the calcium-silicate main layers. This is a consequence of a poor description of the silicate tetrahedra (without polarisability) and the Ca—O interactions, which is reflected in the under-coordination of calcium when considering a cutoff below 3.5 Å (Figs. S5 and S14). However, CSH-FF fails to maintain ordering of the main layer calcium-silicate sheet, while ClayFF successfully maintains the order (Fig. 5). While CSH-FF does not use angle terms for silicate tetrahedra, they are accounted for in ClayFF. This observation underlines the complexity of modeling silicates with empirical interatomic potentials [22].

Further confidence in the predicted tobermorite 14 Å structures comes from the calculated elastic tensor (Table 5). Both Erica FF2 and CementFF4 predict the bulk modulus (K) with very good accuracy. However, to our knowledge there are no individual components of the elastic tensor reported in the literature, and therefore a detailed comparison of the two force fields is not possible.

4.3.2. *Vibrational density of states (v-DOS)*

Power spectra, also known as v-DOS, are obtained from the Fourier transform of the velocity autocorrelation function. v-DOS is not based on selection rules but contains all motions of a system [64]. The calculated spectra are a sum of the infrared (IR) spectrum, the Raman spectrum and all motions that are neither IR nor Raman active [65]. The calculated spectrum reflects the force constants for bond stretching and angle bending in the FF [8]. Since the experimentally obtained spectra hold detailed information on molecular structure and dynamics, with enough precision to analyze the hydrogen bonding patterns, they can be used to test the quality of an FF [89]. The comparison to experimental data not only provides information on the correctness but also the relevance of dipolar polarizability [22].

The MD calculated v-DOS of tobermorite 14 Å are compared to the Ab initio calculation from Vidmer et al. [90] which is in good agreement with experiments (Table S9). Fig. 6 shows the comparison of the total v-DOS, while the projected v-DOS of CementFF4 for each atomic species are given in SI (Fig. S6).

The first half of the first peak (100–200 cm^{-1}) in Fig. 6 corresponds to the deformation of Si tetrahedra and Ca polyhedra, while the second half (200–350 cm^{-1}) corresponds to the deformation of Ca polyhedral only. The second peak (370–520 cm^{-1}) corresponds to the deformation of Si tetrahedra. H_2O vibrations are observed around 510, 650, and 705 cm^{-1}. The vibrational band at 650 cm^{-1} is also assigned to the O—Si—O

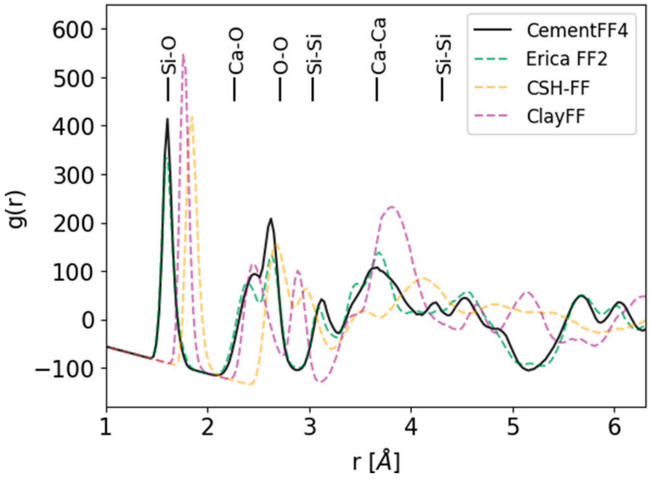

Fig. 4. Pair distribution function calculated for the tobermorite 14 Å structure, as predicted by different FFs. The top lines correspond to the typical distances between atomic species as reported by Bonaccorsi et al. [88].

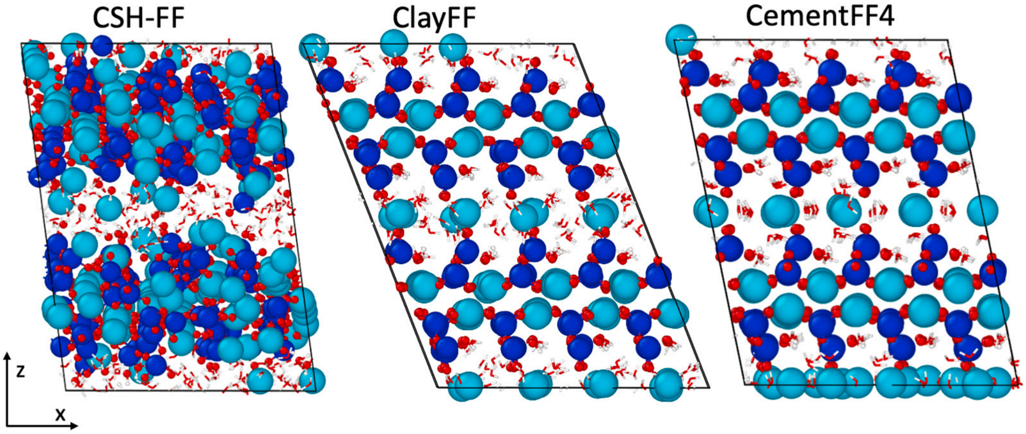

Fig. 5. Snapshot of the tobermorite 14 Å structure simulated with CSH-FF, ClayFF and CementFF4. Color legend: dark blue - Si, turquoise - Ca, red - O, white - H. Water molecules are represented with bonds. (For interpretation of the references to color in this figure legend, the reader is referred to the web version of this article.)

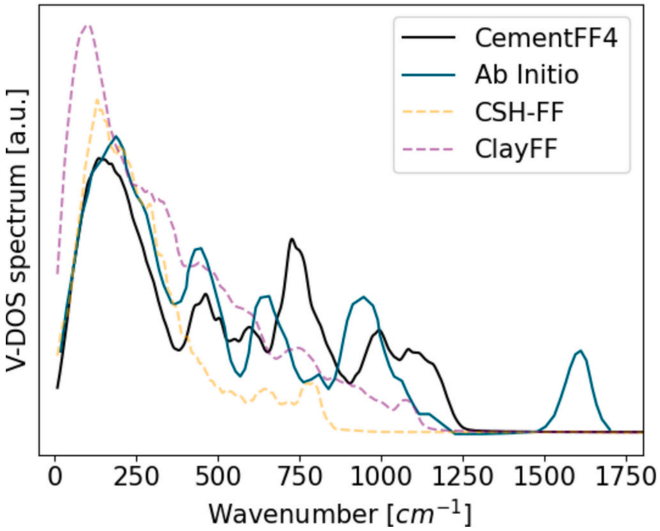

Fig. 6. Total vibrational density of states (v-DOS) for the tobermorite 14 Å structure as predicted by CementFF4 and non-polarizable FFs (ClayFF and CSH-FF) and Ab initio calculation (DFT-GGA) [90]. The projected v-DOS of CementFF4 for each atomic species are shown in Fig. S6.

bending, as seen in the projected v-DOS (SI section 5). The vibrational bands between 815 and 1120 cm^{-1} are due to Si—O stretching. The ab initio contributions in the region around 1200 cm^{-1} are assigned to Si—O stretching and H_2O interactions with O—Si. The ab initio predicted band at 1610 cm^{-1} is assigned to water bending.

The three compared FFs replicate the v-DOS at lower frequencies with good accuracy. These vibrational bands are assigned to the deformation of Si tetrahedra and Ca polyhedral. At higher v-DOS (above 800 cm^{-1}) the non-polarizable FFs ClayFF and CSH-FF poorly or do not at all replicate the vibrational bands. These vibrational bands are assigned to Si—O stretching which further supports the importance of polarizability for the correct description of silicates [22]. The vibrational band of water bending at 1610 cm^{-1} is absent for all FFs, since they all use rigid water models.

In conclusion, we showed that CementFF4 yields energetically stable calculations over long simulation times. CementFF4 also replicates the structural, mechanical and vibrational properties of tobermorite 14 Å structure with good agreement with experimental and ab initio data reported in the literature.

4.3.3. *Zn-C-S-H*

Finally, we compare CementFF4 with a DFT calculated C-S-H structure. The chosen structure is taken from Morales et al. [12], who investigated the incorporation of zinc into the C-S-H structure. The structure is a C-S-H defective unit cell with a zinc tetrahedra replacing the Q^{2b} silicate. This was shown to be the most common incorporation site of zinc in C-S-H [12]. The tetrahedral coordination of the zinc atom is achieved with two oxygens which are shared with neighboring $Q^{2p,Zn}$ silicates and with two hydroxyl groups, which are pointing into the interlayer. The C-S-H defective unit cell was multiplied in all axis direction to create a super cell of dimensions 4 × 4 × 3 defective unit cells. The details of the simulation are given in the Methods section.

Tables 8 and 9 summarize the comparison of the MD predicted structure with the DFT relaxed structure from Morales et al. [12]. The unit cell parameters are well replicated, with the biggest deviation in the c unit direction (5.3 %). The first peaks of the RDFs show a very good match between the MD and DFT results (Table 9) The full RDFs are shown in Fig. S7 The biggest deviation occurs for the Zn-O distance, which is underpredicted by 4.6 %.

5. Conclusions

The present paper describes the further development and validation of a general purpose full charge polarizable force field for cementitious systems (CementFF4). While inclusion of polarizability is needed for the correct structural description of calcium silicate hydrates, it is shown that care must be taken when equilibrating the systems to prevent a drift of total energy. A methodology for the inclusion of transition metals into the force field is presented and validated with respect to experimental measurements and DFT computations. While the force field correctly predicts the first bond distances of hydroxides, it fails to replicate the long ranger ordering with high accuracy for most hydroxides. This is due to the challenge of modeling hydrogen bonding with classical empirical force fields. The key ionic species of C-S-H (namely Ca^{2+} and OH^{-}) are

Table 8
Calculated unit cell parameters for Zn-C-S-H. DFT results are from Morales et al. [12].

	MD	DFT	Dev %
a	6.67 Å	6.62 Å	0.8 %
b	7.44 Å	7.46 Å	−0.3 %
c	14.59 Å	13.86 Å	5.3 %
α	106.00°	106.34°	−0.3 %
β	95.28°	95.79°	−0.5 %
γ	124.53°	123.01°	1.2 %

Table 9
Comparison of first peak reported radial distribution functions for Zn-C-S-H. DFT results are from Morales et al. [12].

	MD [Å]	DFT [Å]
Zn-O	1.88	1.95
Zn-O_H	1.85–2.2	2.0
Si-O	1.63	1.65
Ca-O	2.35	2.35
Ca-O_H	2.57	2.42–2.58

fitted to the Lennard-Jones potential form, which allows for the use of mixing rules for studying surface phenomena [15]. The Ca^{2+} adsorption on quartz surfaces shows comparable results to an established force field from the literature [81]. The re-adoption of the TIP4P/2005 water model allows for simulations with a wide variety of ionic species in solution [42].

Finally, the force field was validated on the tobermorite 14 Å structure due to its similarity to the calcium silicate hydrate structure. Unit cell parameters as well as atomic distances are in excellent agreement with experimentally reported values. Elastic constants, which are one of the most important properties of materials, are also in very good agreement with experimental values. To access the correctness of the force field at the atomic level the vibrational density of states was calculated and compared to an ab-initio calculated one. Again, the force field performs reasonably well. All key vibrational modes of silicates and calcium are captured. These findings demonstrate that cementitious systems (bulk and surfaces) can be explored using this force field with sufficient accuracy to obtain reliable results.

CRediT authorship contribution statement

Ziga Casar: Writing – review & editing, Writing – original draft, Methodology, Investigation, Formal analysis, Conceptualization. **Tecla Bottinelli Montandon:** Writing – review & editing, Investigation, Formal analysis. **Manuel Cordova:** Writing – review & editing, Investigation. **Karen Scrivener:** Writing – review & editing, Supervision, Resources, Funding acquisition. **Paul Bowen:** Writing – review & editing, Writing – original draft, Methodology, Conceptualization. **Aslam Kunhi Mohamed:** Writing – review & editing, Writing – original draft, Supervision, Methodology, Investigation.

Declaration of competing interest

The authors declare that they have no known competing financial interests or personal relationships that could have appeared to influence the work reported in this paper.

Acknowledgments

Prof. Steve Parker, Dr. Sandra Galmarini, Prof. Milan Předota, Prof. Hegoi Manzano, Prof. Michele Ceriotti, and Laura Mismetti are thanked for all the fruitful discussions regarding the adiabatic core-shell model and the water model. Dr. Denys Biriukov is thanked for sharing the SiO_2 data files and discussing the ion adsorption. The Swiss National Science Foundation is acknowledged for financing the contribution of Ziga Casar (grant no. 179076).

Appendix A. Supplementary data

Supplementary data to this article can be found online at https://doi.org/10.1016/j.cemconres.2024.107708.

Data availability

Data will be made available on request.

References

[1] Q. Liu, Progress and research challenges in concrete durability: ionic transport, electrochemical rehabilitation and service life prediction, RILEM Technical Letters 7 (2022) 98–111, https://doi.org/10.21809/rilemtechlett.2022.158.

[2] E. Duque-Redondo, P.A. Bonnaud, H. Manzano, A comprehensive review of C-S-H empirical and computational models, their applications, and practical aspects, Cem. Concr. Res. 156 (2022) 106784, https://doi.org/10.1016/j.cemconres.2022.106784.

[3] K.L. Scrivener, P. Juilland, P.J.M. Monteiro, Advances in understanding hydration of Portland cement, Cem. Concr. Res. 78 (2015) 38–56, https://doi.org/10.1016/j.cemconres.2015.05.025.

[4] K. Ioannidou, C. Labbez, E. Masoero, A review of coarse grained and mesoscale simulations of C–S–H, Cem. Concr. Res. 159 (2022), https://doi.org/10.1016/j.cemconres.2022.106857.

[5] A. Kunhi Mohamed, A. Bouibes, M. Bauchy, Z. Casar, Molecular modelling of cementitious materials: current progress and benefits, RILEM Technical Letters 7 (2022) 209–219, https://doi.org/10.21809/rilemtechlett.2022.175.

[6] K.L. Scrivener, T. Matschei, F. Georget, P. Juilland, A.K. Mohamed, Advances in hydration and thermodynamics of cementitious systems, Cem. Concr. Res. 174 (2023) 107332, https://doi.org/10.1016/j.cemconres.2023.107332.

[7] A. Kunhi Mohamed, S.A. Weckwerth, R.K. Mishra, H. Heinz, R.J. Flatt, Molecular modeling of chemical admixtures; opportunities and challenges, Cem. Concr. Res. 156 (2022) 106783, https://doi.org/10.1016/j.cemconres.2022.106783.

[8] R.K. Mishra, R.J. Flatt, H. Heinz, Force field for tricalcium silicate and insight into nanoscale properties: cleavage, initial hydration, and adsorption of organic molecules, J. Phys. Chem. C 117 (2013) 10417–10432, https://doi.org/10.1021/jp312815g.

[9] Y. Zhang, Q. Zhou, J.W. Ju, M. Bauchy, New insights into the mechanism governing the elasticity of calcium silicate hydrate gels exposed to high temperature: a molecular dynamics study, Cem. Concr. Res. 141 (2021), https://doi.org/10.1016/j.cemconres.2020.106333.

[10] A. Kumar, B.J. Walder, A. Kunhi Mohamed, A. Hofstetter, B. Srinivasan, A. J. Rossini, K. Scrivener, L. Emsley, P. Bowen, The atomic-level structure of cementitious calcium silicate hydrate, J. Phys. Chem. C 121 (2017) 17188–17196, https://doi.org/10.1021/acs.jpcc.7b02439.

[11] A. Kunhi Mohamed, P. Moutzouri, P. Berruyer, B.J. Walder, J. Siramanont, M. Harris, M. Negroni, S.C. Galmarini, S.C. Parker, K.L. Scrivener, L. Emsley, P. Bowen, The atomic-level structure of cementitious calcium aluminate silicate hydrate, J. Am. Chem. Soc. 142 (2020) 11060–11071, https://doi.org/10.1021/jacs.0c02988.

[12] A. Morales-Melgares, Z. Casar, P. Moutzouri, A. Venkatesh, M. Cordova, A. Kunhi Mohamed, K.L. Scrivener, P. Bowen, L. Emsley, Atomic-level structure of zinc-modified cementitious calcium silicate hydrate, J. Am. Chem. Soc. 144 (2022) 22915–22924, https://doi.org/10.1021/jacs.2c06749.

[13] H. Manzano, S. Moeini, F. Marinelli, A.C.T. Van Duin, F.J. Ulm, R.J.M. Pellenq, Confined water dissociation in microporous defective silicates: mechanism, dipole distribution, and impact on substrate properties, J. Am. Chem. Soc. 134 (2012) 2208–2215, https://doi.org/10.1021/ja209152n.

[14] T. Honorio, Monte Carlo molecular modeling of temperature and pressure effects on the interactions between crystalline calcium silicate hydrate layers, Langmuir 35 (2019) 3907–3916, https://doi.org/10.1021/acs.langmuir.8b04156.

[15] Z. Casar, A. Kunhi Mohamed, P. Bowen, K. Scrivener, Atomic-level and surface structure of calcium silicate hydrate nanofoil, J. Phys. Chem. C 127 (2023) 18652–18661, https://doi.org/10.1021/acs.jpcc.3c03350.

[16] M. Schönlein, J. Plank, A TEM study on the very early crystallization of C-S-H in the presence of polycarboxylate superplasticizers: transformation from initial C-S-H globules to nanofoils, Cem. Concr. Res. 106 (2018) 33–39, https://doi.org/10.1016/j.cemconres.2018.01.017.

[17] A. Kunhi Mohamed, S.C. Parker, P. Bowen, S. Galmarini, An atomistic building block description of C-S-H - towards a realistic C-S-H model, Cem. Concr. Res. 107 (2018) 221–235, https://doi.org/10.1016/j.cemconres.2018.01.007.

[18] E. Duque-Redondo, Y. Kazuo, I. López-Arbeloa, H. Manzano, Cs-137 immobilization in C-S-H gel nanopores, Phys. Chem. Chem. Phys. 20 (2018) 9289–9297, https://doi.org/10.1039/c8cp00654g.

[19] S. Galmarini, P. Bowen, Atomistic simulation of the adsorption of calcium and hydroxyl ions onto portlandite surfaces - towards crystal growth mechanisms, Cem. Concr. Res. 81 (2016) 16–23, https://doi.org/10.1016/j.cemconres.2015.11.008.

[20] S. Galmarini, A. Kunhi Mohamed, P. Bowen, Atomistic simulations of silicate species interaction with portlandite surfaces, J. Phys. Chem. C 120 (2016) 22407–22413, https://doi.org/10.1021/acs.jpcc.6b07044.

[21] D. Hou, T. Li, P. Wang, Molecular dynamics study on the structure and dynamics of NaCl solution transport in the nanometer channel of CASH gel, ACS Sustain. Chem. Eng. 6 (2018) 9498–9509, https://doi.org/10.1021/acssuschemeng.8b02126.

[22] M.H. Müser, S.V. Sukhomlinov, L. Pastewka, Interatomic potentials: achievements and challenges, Adv Phys X 8 (2023) 2093129, https://doi.org/10.1080/23746149.2022.2093129.

[23] R.K. Mishra, A.K. Mohamed, D. Geissbühler, H. Manzano, T. Jamil, R. Shahsavari, A.G. Kalinichev, S. Galmarini, et al., cemff: a force field database for cementitious materials including validations, applications and opportunities, Cem. Concr. Res. 102 (2017) 68–89, https://doi.org/10.1016/j.cemconres.2017.09.003.

[24] R. Shahsavari, R.J.M. Pellenq, F.J. Ulm, Empirical force fields for complex hydrated calcio-silicate layered materials, Phys. Chem. Chem. Phys. 13 (2011) 1002–1011, https://doi.org/10.1039/c0cp00516a.

[25] M. Pouvreau, R.T. Cygan, A.G. Kalinichev, Results and Further Development of the ClayFF Classical Force Field, 2017, https://doi.org/10.1021/acs.jpcc.7b05362.

[26] R.T. Cygan, J.J. Liang, A.G. Kalinichev, Molecular models of hydroxide, oxyhydroxide, and clay phases and the development of a general force field, J. Phys. Chem. B 108 (2004) 1255–1266, https://doi.org/10.1021/jp0363287.

[27] M.F. Döpke, J. Lützenkirchen, O.A. Moultos, B. Siboulet, J.-F. Dufrêche, J. T. Padding, R. Hartkamp, Preferential adsorption in mixed electrolytes confined by charged amorphous silica, J. Phys. Chem. C 123 (2019) 16711–16720, https://doi.org/10.1021/acs.jpcc.9b02975.

[28] Y. Zhou, D. Hou, J. Jiang, P. Wang, Chloride ions transport and adsorption in the nano-pores of silicate calcium hydrate: experimental and molecular dynamics studies, Construct. Build Mater. 126 (2016) 991–1001, https://doi.org/10.1016/j.conbuildmat.2016.09.110.

[29] I. Androniuk, A.G. Kalinichev, Molecular dynamics simulation of the interaction of uranium (VI) with the C–S–H phase of cement in the presence of gluconate, Appl. Geochem. 113 (2020) 104496, https://doi.org/10.1016/j.apgeochem.2019.104496.

[30] I. Androniuk, C. Landesman, P. Henocq, A.G. Kalinichev, Adsorption of gluconate and uranyl on C-S-H phases: combination of wet chemistry experiments and molecular dynamics simulations for the binary systems, Phys. Chem. Earth 99 (2017) 194–203, https://doi.org/10.1016/j.pce.2017.05.005.

[31] A. Sam, S.K. Kannam, R. Hartkamp, S.P. Sathian, Water flow in carbon nanotubes: the effect of tube flexibility and thermostat, Journal of Chemical Physics 146 (2017), https://doi.org/10.1063/1.4985252.

[32] E. Galicia-Andrés, D. Petrov, M.H. Gerzabek, C. Oostenbrink, D. Tunega, Polarization effects in simulations of kaolinite–water interfaces, Langmuir 35 (2019) 15086–15099, https://doi.org/10.1021/acs.langmuir.9b02945.

[33] H. Heinz, T.J. Lin, R. Kishore Mishra, F.S. Emami, Thermodynamically consistent force fields for the assembly of inorganic, organic, and biological nanostructures: the INTERFACE force field, Langmuir 29 (2013) 1754–1765, https://doi.org/10.1021/la3038846.

[34] K. Kanhaiya, M. Nathanson, P.J. in't Veld, C. Zhu, I. Nikiforov, E.B. Tadmor, Y. K. Choi, W. Im, R.K. Mishra, H. Heinz, Accurate force fields for atomistic simulations of oxides, hydroxides, and organic hybrid materials up to the micrometer scale, J Chem Theory Comput 19 (2023) 8293–8322, https://doi.org/10.1021/acs.jctc.3c00750.

[35] M. Valavi, Z. Casar, A. Kunhi, P. Bowen, S. Galmarini, Molecular dynamic simulations of cementitious systems using a newly developed force field suite ERICA FF, Cem. Concr. Res. 154 (2022) 106712, https://doi.org/10.1016/j.cemconres.2022.106712.

[36] T.-C. Lim, Alignment of Buckingham parameters to generalized Lennard-Jones potential functions, Z. Naturforsch. 64a (2009) 200–204.

[37] P.J. Mitchell, D. Fincham, Shell model simulations by adiabatic dynamics, J. Phys. Condens. Matter 5 (1993) 1031–1038, https://doi.org/10.1088/0953-8984/5/8/006.

[38] Y. Wu, H.L. Tepper, G.A. Voth, Flexible simple point-charge water model with improved liquid-state properties, Journal of Chemical Physics 124 (2006), https://doi.org/10.1063/1.2136877.

[39] G.V. Lewis, C.R.A. Catlow, W.C. Mackrodt, R.F. Stewart, W.C. Mackrodt, R. F. Stewart, C.R.A. Catlow, A.M. Stoneham, Potential models for ionic oxides, J. Phys. C Solid State Phys. 18 (1985) 1149–1161, https://doi.org/10.1088/0022-3719/18/6/010.

[40] J.L.F. Abascal, C. Vega, A general purpose model for the condensed phases of water: TIP4P/2005, Journal of Chemical Physics 123 (2005), https://doi.org/10.1063/1.2121687.

[41] M. Předota, D. Biriukov, Electronic continuum correction without scaled charges, J. Mol. Liq. 314 (2020), https://doi.org/10.1016/j.molliq.2020.113571.

[42] M.F. Döpke, O.A. Moultos, R. Hartkamp, On the transferability of ion parameters to the TIP4P/2005 water model using molecular dynamics simulations, Journal of Chemical Physics 152 (2020), https://doi.org/10.1063/1.5124448.

[43] C.L. Freeman, J.H. Harding, D.J. Cooke, J.A. Elliott, J.S. Lardge, D.M. Duffy, New forcefields for modeling biomineralization processes, J. Phys. Chem. C 111 (2007) 11943–11951, https://doi.org/10.1021/jp071887p.

[44] A. Tilocca, N.H. De Leeuw, A.N. Cormack, Shell-model molecular dynamics calculations of modified silicate glasses, Phys Rev B 73 (2006) 104209, https://doi.org/10.1103/PhysRevB.73.104209.

[45] N.H. De Leeuw, Computer simulations of surfaces and interfaces: a case study of the hydration and dissolution of α-quartz SiO 2 (4) (1992) 66–102.

[46] J.N. Israelachvili, Interactions involving the polarization of molecules, in: Intermolecular and Surface Forces, Elsevier, 2011, pp. 91–106, https://doi.org/10.1016/B978-0-12-375182-9.10005-3.

[47] I. Leontyev, A. Stuchebrukhov, Accounting for electronic polarization in non-polarizable force fields, Phys. Chem. Chem. Phys. 13 (2011) 2613–2626, https://doi.org/10.1039/c0cp01971b.

[48] G. Lamoureux, B. Roux, Modeling induced polarization with classical Drude oscillators: theory and molecular dynamics simulation algorithm, Journal of Chemical Physics 119 (2003) 3025–3039, https://doi.org/10.1063/1.1589749.

[49] P. Mark, L. Nilsson, Structure and dynamics of the TIP3P, SPC, and SPC/E water models at 298 K, J. Phys. Chem. A 105 (2001) 9954–9960, https://doi.org/10.1021/jp003020w.

[50] A.P. Thompson, H.M. Aktulga, R. Berger, D.S. Bolintineanu, W.M. Brown, P. S. Crozier, P.J. in't Veld, A. Kohlmeyer, et al., LAMMPS - a flexible simulation tool for particle-based materials modeling at the atomic, meso, and continuum scales, Comput. Phys. Commun. 271 (2022) 108171, https://doi.org/10.1016/j.cpc.2021.108171.

[51] C. Vega, J.L.F. Abascal, Simulating water with rigid non-polarizable models: a general perspective, Phys. Chem. Chem. Phys. 13 (2011) 19663–19688, https://doi.org/10.1039/c1cp22168j.

[52] I.M. Zeron, J.L.F. Abascal, C. Vega, A force field of Li+, Na+, K+, Mg2+, Ca2+, Cl-, and S O 4 2 - in aqueous solution based on the TIP4P/2005 water model and scaled charges for the ions, J. Chem. Phys. 151 (2019), https://doi.org/10.1063/1.5121392.

[53] T.R. Underwood, H.C. Greenwell, The water-alkane interface at various NaCl salt concentrations: a molecular dynamics study of the readily available force fields, Sci. Rep. 8 (2018), https://doi.org/10.1038/s41598-017-18633-y.

[54] S. Yamaguchi, T. Takayama, T. Otosu, Appraisal of TIP4P-type models at water surface, J. Chem. Phys. 159 (2023), https://doi.org/10.1063/5.0171999.

[55] X. Wang, S. Ramírez-Hinestrosa, J. Dobnikar, D. Frenkel, The Lennard-Jones potential: when (not) to use it, Phys. Chem. Chem. Phys. 22 (2020) 10624–10633, https://doi.org/10.1039/c9cp05445f.

[56] P. Li, L.F. Song, K.M. Merz, Parameterization of highly charged metal ions using the 12-6-4 LJ-type nonbonded model in explicit water, Journal of Physical Chemistry B 119 (2015) 883–895, https://doi.org/10.1021/jp505875v.

[57] M. Arab, D. Bougeard, K.S. Smirnov, Molecular dynamics study of the structure and dynamics of Zn2+ ion in water, Chem. Phys. Lett. 379 (2003) 268–276, https://doi.org/10.1016/S0009-2614(03)01252-1.

[58] H.A. Lorentz, Ueber die Anwendung des Satzes vom Virial in der kinetischen Theorie der Gase, Ann. Phys. 248 (1881) 127–136, https://doi.org/10.1002/andp.18812480110.

[59] D. Berthelot, Sur le melange des gaz, C. R. Hebd. Seances Acad. Sci. 126 (1898) 1703–1855.

[60] J. Delhommelle, P. Millié, Inadequacy of the Lorentz-Berthelot combining rules for accurate predictions of equilibrium properties by molecular simulation, Mol. Phys. 99 (2001) 619–625, https://doi.org/10.1080/00268970010020041.

[61] S. Mamatkulov, M. Fyta, R.R. Netz, Force fields for divalent cations based on single-ion and ion-pair properties, J. Chem. Phys. 138 (2013) 024505, https://doi.org/10.1063/1.4772808.

[62] P. Virtanen, R. Gommers, T.E. Oliphant, M. Haberland, T. Reddy, D. Cournapeau, E. Burovski, P. Peterson, et al., SciPy 1.0: fundamental algorithms for scientific computing in Python, Nat. Methods 17 (2020) 261–272, https://doi.org/10.1038/s41592-019-0686-2.

[63] W. Smith, C.W. Yong, P.M. Rodger, DL_POLY: application to molecular simulation, Mol. Simul. 28 (2002) 385–471, https://doi.org/10.1080/08927020290018769.

[64] M. Brehm, M. Thomas, S. Gehrke, B. Kirchner, TRAVIS—a free analyzer for trajectories from molecular simulation, Journal of Chemical Physics 152 (2020), https://doi.org/10.1063/5.0005078.

[65] M. Brehm, B. Kirchner, TRAVIS - a free analyzer and visualizer for Monte Carlo and molecular dynamics trajectories, J. Chem. Inf. Model. 51 (2011) 2007–2023, https://doi.org/10.1021/ci200217w.

[66] A. Jain, S.P. Ong, G. Hautier, W. Chen, W.D. Richards, S. Dacek, S. Cholia, D. Gunter, D. Skinner, G. Ceder, K.A. Persson, Commentary: the materials project: a materials genome approach to accelerating materials innovation, APL Mater. 1 (2013), https://doi.org/10.1063/1.4812323.

[67] P. Giannozzi, O. Baseggio, P. Bonfà, D. Brunato, R. Car, I. Carnimeo, C. Cavazzoni, S. De Gironcoli, P. Delugas, et al., Quantum ESPRESSO toward the exascale, Journal of Chemical Physics 152 (2020), https://doi.org/10.1063/5.0005082.

[68] P. Giannozzi, S. Baroni, N. Bonini, M. Calandra, R. Car, C. Cavazzoni, D. Ceresoli, G.L. Chiarotti, et al., QUANTUM ESPRESSO: a modular and open-source software project for quantum simulations of materials, J. Phys. Condens. Matter 21 (2009) 395502, https://doi.org/10.1088/0953-8984/21/39/395502.

[69] J.P. Perdew, K. Burke, M. Ernzerhof, Generalized gradient approximation made simple, Phys. Rev. Lett. 77 (1996) 3865–3868, https://doi.org/10.1103/PhysRevLett.77.3865.

[70] S. Grimme, Semiempirical GGA-type density functional constructed with a long-range dispersion correction, J. Comput. Chem. 27 (2006) 1787–1799, https://doi.org/10.1002/jcc.20495.

[71] G. Kresse, D. Joubert, From ultrasoft pseudopotentials to the projector augmented-wave method, Phys. Rev. B 59 (1999) 1758–1775, https://doi.org/10.1103/PhysRevB.59.1758.

[72] A. Dal Corso, Pseudopotentials periodic table: from H to Pu, Comput. Mater. Sci. 95 (2014) 337–350, https://doi.org/10.1016/j.commatsci.2014.07.043.

[73] H.J. Monkhorst, J.D. Pack, Special points for Brillouin-zone integrations, Phys Rev B 13 (1976) 5188–5192, https://doi.org/10.1103/PhysRevB.13.5188.

[74] R. Golesorkhtabar, P. Pavone, J. Spitaler, P. Puschnig, C. Draxl, ElaStic: a tool for calculating second-order elastic constants from first principles, Comput. Phys. Commun. 184 (2013) 1861–1873, https://doi.org/10.1016/j.cpc.2013.03.010.

[75] S. Hajilar, B. Shafei, Assessment of structural, thermal, and mechanical properties of portlandite through molecular dynamics simulations, J. Solid State Chem. 244 (2016) 164–174, https://doi.org/10.1016/j.jssc.2016.09.026.

[76] D.A. Kulik, G.D. Miron, B. Lothenbach, A structurally-consistent CASH+ sublattice solid solution model for fully hydrated C-S-H phases: thermodynamic basis, methods, and Ca-Si-H2O core sub-model, Cem. Concr. Res. 151 (2022) 106585, https://doi.org/10.1016/j.cemconres.2021.106585.

[77] M. De Jong, W. Chen, T. Angsten, A. Jain, R. Notestine, A. Gamst, M. Sluiter, C. K. Ande, S. Van Der Zwaag, J.J. Plata, C. Toher, S. Curtarolo, G. Ceder, K. A. Persson, M. Asta, Charting the complete elastic properties of inorganic crystalline compounds, Sci Data 2 (2015), https://doi.org/10.1038/sdata.2015.9.

[78] G. Clavier, N. Desbiens, E. Bourasseau, V. Lachet, N. Brusselle-Dupend, B. Rousseau, Computation of elastic constants of solids using molecular simulation: comparison of constant volume and constant pressure ensemble methods, Mol Simul 43 (2017) 1413–1422, https://doi.org/10.1080/08927022.2017.1313418.

[79] S. Speziale, H.J. Reichmann, F.R. Schilling, H.R. Wenk, P.J.M. Monteiro, Determination of the elastic constants of portlandite by Brillouin spectroscopy,

Cem. Concr. Res. 38 (2008) 1148–1153, https://doi.org/10.1016/j.cemconres.2008.05.006.

[80] J.L. Laugesen, Density functional calculations of elastic properties of portlandite, Ca(OH)2, Cem. Concr. Res. 35 (2005) 199–202, https://doi.org/10.1016/j.cemconres.2004.07.036.

[81] M. Bischoff, D. Biriukov, M. Předota, A. Marchioro, Second harmonic scattering reveals ion-specific effects at the SiO2 and TiO2 nanoparticle/aqueous interface, J. Phys. Chem. C 125 (2021) 25261–25274, https://doi.org/10.1021/acs.jpcc.1c07191.

[82] D. Biriukov, O. Kroutil, M. Předota, Modeling of solid-liquid interfaces using scaled charges: rutile (110) surfaces, Phys. Chem. Chem. Phys. 20 (2018) 23954–23966, https://doi.org/10.1039/C8CP04535F.

[83] S.V. Churakov, C. Labbez, L. Pegado, M. Sulpizi, Intrinsic acidity of surface sites in calcium silicate hydrates and its implication to their electrokinetic properties, J. Phys. Chem. C 118 (2014) 11752–11762, https://doi.org/10.1021/jp502514a.

[84] C. Labbez, B. Jönsson, I. Pochard, A. Nonat, B. Cabane, Surface charge density and electrokinetic potential of highly charged minerals: experiments and Monte Carlo simulations on calcium silicate hydrate, J. Phys. Chem. B 110 (2006) 9219–9230, https://doi.org/10.1021/jp057096+.

[85] A. Marchioro, M. Bischoff, C. Lütgebaucks, D. Biriukov, M. Předota, S. Roke,
A. Marchioro, M. Bischoff, C. Lütgebaucks, D. Biriukov, M. Předota, S. Roke,
Surface characterization of colloidal silica nanoparticles by second harmonic scattering: quantifying the surface potential and interfacial water order, J. Phys. Chem. C 123 (2019) 20393–20404, https://doi.org/10.1021/acs.jpcc.9b05482.

[86] I.G. Richardson, Model structures for C-(A)-S-H(I), Acta Crystallogr B Struct Sci Cryst Eng Mater 70 (2014) 903–923, https://doi.org/10.1107/S2052520614021982.

[87] K. Garbev, G. Beuchle, M. Bornefeld, L. Black, P. Stemmermann, Cell dimensions and composition of nanocrystalline calcium silicate hydrate solid solutions. Part 1: synchrotron-based X-ray diffraction, J. Am. Ceram. Soc. 91 (2008) 3005–3014, https://doi.org/10.1111/j.1551-2916.2008.02484.x.

[88] E. Bonaccorsi, S. Merlino, A.R. Kampf, The crystal structure of tobermorite 14 Å (plombierite), a C-S-H phase, J. Am. Ceram. Soc. 88 (2005) 505–512, https://doi.org/10.1111/j.1551-2916.2005.00116.x.

[89] H. Henschel, A.T. Andersson, W. Jespers, M. Mehdi Ghahremanpour, D. Van Der Spoel, Theoretical infrared spectra: quantitative similarity measures and force fields, J. Chem. Theory Comput. 16 (2020) 3307–3315, https://doi.org/10.1021/acs.jctc.0c00126.

[90] A. Vidmer, G. Sclauzero, A. Pasquarello, Infrared spectra of jennite and tobermorite from first-principles, Cem. Concr. Res. 60 (2014) 11–23, https://doi.org/10.1016/j.cemconres.2014.03.004.